

Seeds of Life in Space (SOLIS)

X. Interstellar complex organic molecules in the NGC 1333 IRAS 4A outflows[★]

M. De Simone¹, C. Codella^{2,1}, C. Ceccarelli¹, A. López-Sepulcre^{3,1}, A. Witzel¹, R. Neri³, N. Balucani^{4,1}, P. Caselli⁵, C. Favre¹, F. Fontani², B. Lefloch¹, J. Ospina-Zamudio¹, J. E. Pineda⁵, and V. Taquet²

¹ Univ. Grenoble Alpes, CNRS, IPAG, 38000 Grenoble, France
e-mail: marta.desimone@univ-grenoble-alpes.fr

² INAF, Osservatorio Astrofisico di Arcetri, Largo E. Fermi 5, 50125 Firenze, Italy

³ Institut de Radioastronomie Millimétrique (IRAM), 300 rue de la Piscine, 38400 Saint-Martin d'Hères, France

⁴ Dipartimento di Chimica, Biologia e Biotecnologie, Università degli Studi di Perugia, Perugia 06123, Italy

⁵ Max-Planck-Institut für extraterrestrische Physik (MPE), Giessenbachstrasse 1, 85748 Garching, Germany

Received 28 October 2019 / Accepted 12 June 2020

ABSTRACT

Context. The interstellar complex organic molecules (iCOMs) are C-bearing molecules containing at least six atoms; two main proposals for their formation are suggested: a direct formation in the icy mantle of the dust grains and formation through the reaction in gas phase of released grain mantle species. The shocked gas along outflows driven by low-mass protostars is a unique environment to study how the iCOMs can be formed as the composition of the dust mantles is sputtered into the gas phase.

Aims. The chemical richness in shocked material associated with low-mass protostellar outflows has been so far studied in the prototypical L1157 blue-shifted outflow to investigate the iCOM formation routes. To understand whether the case of L1157-B1 is unique, we imaged and studied the IRAS 4A outflows in the NGC 1333 star forming region.

Methods. We used the Northern Extended Millimeter Array interferometer as part of the IRAM Seeds Of Life in Space (SOLIS) Large Program to image the large-scale bipolar outflows driven by the IRAS 4A system in the 3 mm band, and we compared the observation with the GRAINOBLE+ astrochemical model.

Results. We report the first detection, in the IRAS 4A outflows, of several iCOMs: six lines of methanol (CH₃OH), eight of acetaldehyde (CH₃CHO), one of formamide (NH₂CHO), and four of dimethyl ether (CH₃OCH₃), all sampling upper excitation energy up to ~30 K. We found a significant chemical differentiation between the southeast outflow driven by the IRAS 4A1 protostar, showing a richer molecular content, and the north-southwest one driven by the IRAS 4A2 hot corino. The CH₃OH/CH₃CHO abundance ratio is lower by a factor of ~4 in the former; furthermore, the ratio in the IRAS 4A outflows is lower by a factor of ~10 with respect to the values found in different hot corinos.

Conclusions. After L1157-B1, the IRAS 4A outflow is now the second outflow to show an evident chemical complexity. Given that CH₃OH is a grain surface species, the astrochemical gas-phase model run with GRAINOBLE+ reproduced our observation assuming that acetaldehyde is formed mainly through the gas-phase reaction of the ethyl radical (CH₃CH₂) and atomic oxygen. Furthermore, the chemical differentiation between the two outflows suggests that the IRAS 4A1 outflow is likely younger than that of the IRAS 4A2. Further investigation is needed to constrain the age of the outflow. In addition, observation of even younger shocks are necessary. In order to provide strong constraints on the CH₃CHO formation mechanisms it would be interesting to observe CH₃CH₂, but given that its frequencies are not known, future spectroscopic studies on this species are needed.

Key words. astrochemistry – instrumentation: interferometers – stars: formation – ISM: jets and outflows – ISM: molecules – ISM: individual objects: NGC 1333 IRAS 4A

1. Introduction

Since the discovery of interstellar complex organic molecules (iCOMs¹, molecules containing carbon and at least six atoms: Herbst & van Dishoeck 2009; Ceccarelli et al. 2017) in solar-type protostars (Cazaux et al. 2003), the question whether they had a role in the appearance of life on Earth (and elsewhere in the Universe) has been raised. Although they are extremely

small molecules compared to biotic molecules, iCOMs may have provided the bricks to build them. The presence of amino acids in meteorites and comets has certainly revived this possibility (e.g., Pizzarello et al. 2006; Elsila et al. 2009; Altwegg et al. 2016).

In addition to their possible role in the emergence of life, iCOMs represent a challenge for astrochemistry as their synthesis is all but obvious. Nowadays, two main paradigms are invoked (see, e.g., Herbst 2017) that argue that iCOMs are either synthesized on the grain surfaces (e.g., Garrod & Herbst 2006; Garrod 2008) or in the gas phase (e.g., Millar et al. 1991; Balucani et al. 2015; Skouteris et al. 2018). As a starting point, both pathways have the formation of simple hydrogenated molecules on dust grain mantles during the pre-stellar phase. Constraining which of the two ways to synthesize iCOMs is more efficient and where

* The reduced images are only available at the CDS via anonymous ftp to [cdsarc.u-strasbg.fr](ftp://cdsarc.u-strasbg.fr) (130.79.128.5) or via <http://cdsarc.u-strasbg.fr/viz-bin/cat/J/A+A/640/A75>

¹ We added “i” to the commonly used COMs acronym in order to be clear that these molecules are only complex in the interstellar context, contrary to what chemists consider complex in the terrestrial context.

the iCOMs form is not a simple task. Many methods have been used, from the comparison of the iCOM measured abundances in hot cores and hot corinos with model predictions to their measured deuterium fractionation (Turner 1990; Ceccarelli et al. 1998; Coutens et al. 2016; Skouteris et al. 2017; Jørgensen et al. 2018).

One method that turned out to be very efficient is to compare observations toward low-mass outflow shocks with model predictions (Codella et al. 2017). The advantage of this method is that the outflow shocks provide the time dependence as an additional constraint. Once the iCOM emission has been localized in a precise region (thanks to high spatial resolution observations), it is possible to identify in that region a shock event that corresponds naturally to a precise kinematical age (e.g., Gueth et al. 1996; Podio et al. 2016). After the passage of the shock, the chemistry in the shocked region evolves with time. Therefore, the comparison of observed iCOM abundances with model predictions provides strong constraints on the formation routes because it is possible to make the comparison at the precise kinematical shock age. This method was successfully applied in the L1157-B1 outflow shock to constrain the formation route of formamide. Thanks to interferometric high spatial resolution observations, Codella et al. (2017) found a difference in the spatial distribution between acetaldehyde and formamide emission, and consequently they were able to constrain the formamide formation as being due to gas-phase reactions. We note that these conclusions apply to L1157-B1 only. Given its power, it is important to apply the same method to other iCOMs and other protostellar shocks.

Unfortunately, there are very few observations of iCOMs in low-mass protostellar shocks. To our knowledge, iCOMs other than methanol have been detected only toward a handful of objects: several iCOMs toward L1157-B1 (Arce et al. 2008; Lefloch et al. 2017), formamide toward L1157-B2 (Mendoza et al. 2014), acetaldehyde toward IRAS 2A and IRAS 4A (Holdship et al. 2019), and acetaldehyde and dimethyl ether toward SMM4-W (Öberg et al. 2011). However, it is worth noting that all these works refer to single-dish observations at relatively low spatial angular resolution and are, by definition, unable to disentangle the different spatial distribution of iCOMs caused by the age of the shocks, so that the method described above cannot be used.

In this work, we present new high spatial observations toward the two outflows from IRAS 4A. This source is one of the targets of the Seeds Of Life In Space (SOLIS) Large Program (Ceccarelli et al. 2017) at the IRAM/NORthern Extended Millimeter Array (NOEMA) interferometer, whose goal is to investigate iCOM chemistry during the earliest formation phases of solar-type stellar systems. The observations targeted three iCOMs in addition to methanol (CH_3OH): acetaldehyde (CH_3CHO), dimethyl ether (CH_3OCH_3), and formamide (NH_2CHO). All these iCOMs were detected in our data set. The detection of different iCOMs in the outflowing gas of IRAS 4A with high spatial resolution observations allows us to apply the method of model-observations comparison described above.

The article is organized as follows: we first give the IRAS 4A source background in Sect. 2, then present the observations in Sect. 3, and the results in Sect. 4; we derive the abundance ratios of the detected iCOMs in different positions of the IRAS 4A outflows in Sect. 5, and the model predictions to interpret them in Sect. 6; in Sect. 7 we discuss what our new observations imply, and finally in Sect. 8 we summarize our work.

2. IRAS 4A: source background

IRAS 4A is part of the multiple system IRAS 4, located at a distance of 299 ± 15 pc in the NGC 1333 region of the Perseus complex (Zucker et al. 2018). The system IRAS 4A is constituted of four objects: 4A, 4B, 4B', and 4C (Lay et al. 1995; Looney et al. 2000; Smith et al. 2000; Di Francesco et al. 2001; Choi 2001). IRAS 4A is itself a binary system with two Class 0 objects, 4A1 and 4A2, separated by $1''.8$ (~ 540 au; Looney et al. 2000; Santangelo et al. 2015; López-Sepulcre et al. 2017; Maury et al. 2019). At the millimeter wavelengths, 4A1 is three times brighter than 4A2. However, their respective luminosity is unknown since they are not resolved in the submillimeter to IR wavelengths where the luminosity peak lies. The bolometric luminosity of the whole IRAS 4A system is $9.1 L_\odot$ (Kristensen et al. 2012; Karska et al. 2013).

IRAS 4A is the second hot corino ever discovered (Bottinelli et al. 2004), after IRAS 16293-2422 (Cazaux et al. 2003). Interferometric IRAM/PdBI (Plateau de Bure Interferometer, now evolved into NOEMA) observations later suggested that iCOM emission originates from 4A2 rather than 4A1 (Taqet et al. 2015; De Simone et al. 2017). More recently, López-Sepulcre et al. (2017) obtained high-resolution ($\sim 0''.5$) ALMA images of IRAS 4A, and confirmed the huge contrast between 4A1 and 4A2: while 4A2 shows hot corino activity with enriched iCOM emission, no sign of iCOMs is detected in 4A1. López-Sepulcre et al. (2017) suggest that either 4A1 does not host a hot corino or, alternatively, the hot corino size is less than ~ 15 au (after scaling to 299 pc the distance adopted by López-Sepulcre et al. 2017), namely six times smaller than the 4A2 corino. However, thanks to recent observations at centimeter wavelengths performed with the Jansky Very Large Array (VLA), De Simone et al. (2020) have detected, for the first time, a clearly disentangled methanol emission toward both 4A1 and 4A2 revealing the 4A1 hot corino region that was obscured by the dust at millimeter wavelengths.

As for many Class 0 protostars, IRAS 4A is associated with a spectacular large-scale (a few arcminutes) bipolar outflow observed with several tracers, such as CO, SiO, SO, HCN (Blake et al. 1995; Lefloch et al. 1998; Choi 2005; Choi et al. 2011). Choi (2005) clearly traced the high-velocity component with SiO emission using VLA observations at $2''$ spatial resolution. From their map it is possible to distinguish two different blue-shifted lobes toward the south and only one northern red-shifted lobe with a peculiar bending toward the northeast at $20''$ from the protostars. Using IRAM/PdBI high spatial resolution observations ($<1''$), Santangelo et al. (2015) mapped the outflows at lower scale ($\sim 30''$) with respect to the SiO map from Choi (2005). They traced different velocity components (from ~ 10 to ~ 60 km s $^{-1}$) using CO, SiO, and SO as tracers. With their study Santangelo et al. (2015) were able to clearly disentangle the two southern lobes, revealing a fast collimated jet associated with bright H_2 emission and driven by 4A1 (southeast lobe) and a slower and precessing jet driven by 4A2 (southwest lobe). Furthermore, the jets present different morphologies: the 4A2 jet shows a large spatial extent and an S-shaped pattern on small scales, probably due to jet precession; the 4A1 jet is faster, covers a smaller extent ($\sim 15''$), and presents as C-shaped tilted toward the east of 4A1.

Thanks to a detailed study on sulfur species using interferometric observations, for the first time Taquet et al. (2020) were able to distinguish the outflow driven by 4A1 from the one driven by 4A2 also in the northern lobe.

The left panel of Fig. 1 summarizes the situation: it shows the distribution of the dust cores at large scale, traced by the

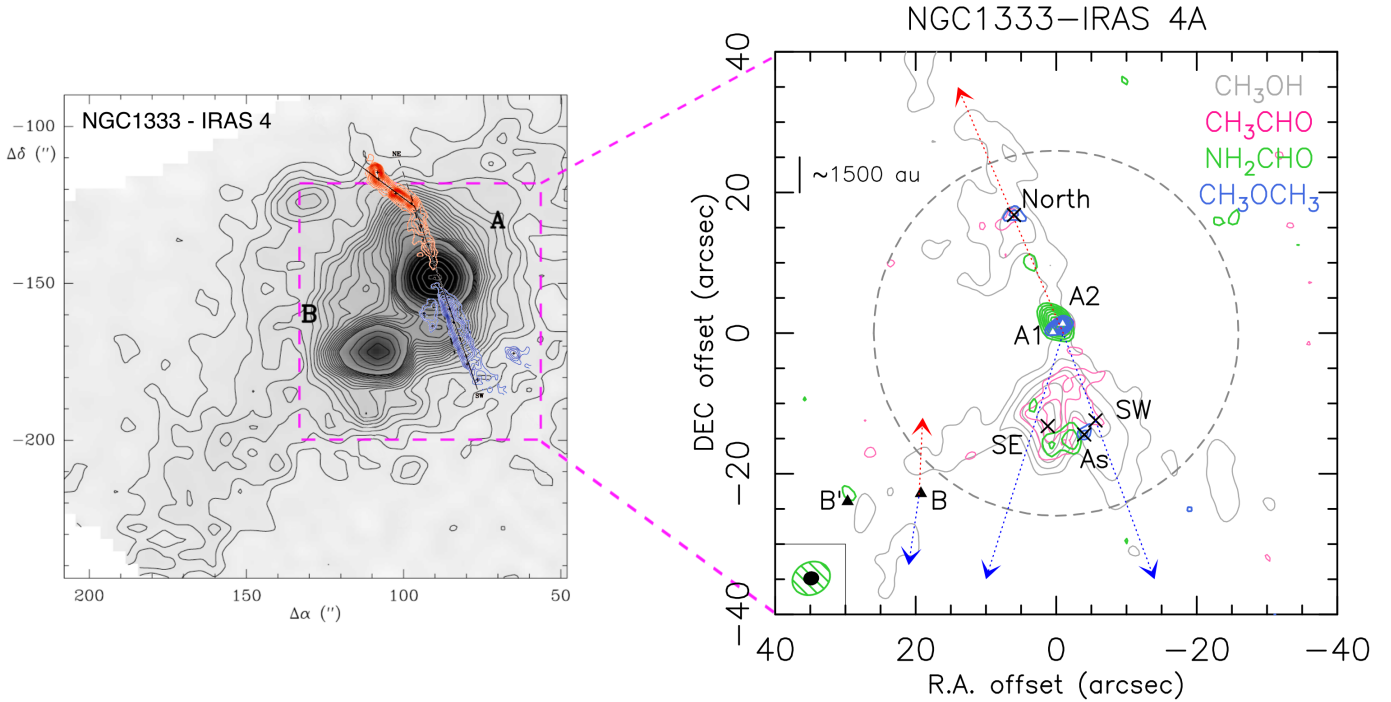


Fig. 1. *Left:* overlap of the contour map of the 1.25 mm continuum emission from NGC 1333 IRAS 4 region in Perseus, observed with the IRAM 30 m antenna (Lefloch et al. 1998), with the map of SiO line (VLA observations; Choi 2005). Axes offsets are in arcseconds from SVS 13 ($\alpha(2000) = 03^{\text{h}}29^{\text{m}}3.9$ and $\delta(2000) = 31^{\circ}16'8''$). *Right:* zoomed-in image of the IRAS 4A system with NOEMA-SOLIS observations. Axes offsets are in arcseconds from IRAS 4A. A spatial separation of $5''$ correspond to ~ 1500 au at a distance of 299 pc (Zucker et al. 2018). The white triangles give the position of the sources 4A1 and 4A2, while the black triangles give the position of the sources 4B and 4B' (coordinates in Table 2). The black crosses give the analyzed positions in the outflows (SE, SW, North, and As; coordinates in Table 2). The dashed blue and red arrows indicate the direction of the blue- and red-shifted 4B outflow (from the HCN observations of Choi 2001) and of the 4A outflow. The contour map represents the iCOMs emission at 3 mm in the IRAS 4A outflows (this work). For all the iCOMs the contours start at 3σ with steps of 1σ , except for methanol whose contours have steps of 20σ . The emission distribution is the following: 1) methanol (CH_3OH in gray), integrated over the transitions $2_{0,2} - 1_{0,1}$ A, $2_{0,2} - 1_{0,1}$ E, and $2_{-1,2} - 1_{-1,1}$ E with $\sigma = 75$ mJy beam $^{-1}$ km s $^{-1}$; 2) acetaldehyde (CH_3CHO , in magenta), here in the $5_{0,5} - 4_{0,4}$ A emission with $\sigma = 11$ mJy beam $^{-1}$ km s $^{-1}$; 3) formamide (NH_2CHO , in green), $4_{1,4} - 3_{1,3}$ emission with $\sigma = 10$ mJy beam $^{-1}$ km s $^{-1}$; dimethyl ether (CH_3OCH_3 , in blue), $4_{1,4} - 3_{0,3}$ emission with $\sigma = 9$ mJy beam $^{-1}$ km s $^{-1}$. The synthesized beams for the formamide line (green, $\sim 4''$) and for the other species (black, $\sim 2''$) are indicated in the lower left corner. The primary beam ($\sim 52''$) is shown as a dashed gray circle.

Table 1. Characteristics of the SOLIS WideX backend setups.

Setup	Frequency range (GHz) [GHz]	Spectral resolution [km s $^{-1}$]	Spectral resolution [MHz]	Spatial resolution [$''$]	Spatial resolution [au] ^(a)	Synthesized beam [$'' \times ''$ ($^\circ$)]	Primary beam [$''$]	Primary beam [au] ^(a)
1	80.8–84.4	7	2	4	~ 1200	4.5×3.5 (27)	$61'4$	$\sim 2 \times 10^4$
3	95.5–99.5	6	2	4	~ 1200	2.2×1.9 (96)	$59'2$	$\sim 2 \times 10^4$

Notes. ^(a)Computed at the distance of the NGC 1333 region (~ 299 pc; Zucker et al. 2018).

continuum at 1.3 mm using the IRAM 30m (Lefloch et al. 1998), together with large-scale high-velocity outflow traced by the SiO (1-0) line using the VLA interferometer (Choi 2005).

3. Observations

IRAS 4A was observed with the IRAM/NOEMA interferometer during several tracks in June and September 2016. Two frequency setups were used, called 1 and 3 in Ceccarelli et al. (2017, Table 4), centered at ~ 82 and ~ 97 GHz, respectively. The array was used in configurations D and C with baselines from 15 m to 304 m for Setup 3 and from 16 to 240 m for Setup 1. Here, we present the data obtained using the WideX backend, whose characteristics are summarized in Table 1.

The phase center is on the IRAS 4A1 source, whose coordinates are listed in Table 2. The bandpass was calibrated on 3C454.3 and 3C84, while the flux was calibrated using MWC349 and LKHA101. The calibration of phase and amplitude was done observing 0333+321. The system temperatures typically ranged between 50 and 200 K. The calibration error associated with the absolute flux is $\leq 15\%$. The data were reduced using the packages CLIC and MAPPING of the GILDAS² software collection. The data were self-calibrated in phase only; the self-calibration solutions were applied to the data spectral cube, which was then cleaned. A continuum map (see Fig. 2) was obtained by averaging line-free channels from the self-calibrated data. The resulting synthesized beam is $2'2 \times 1'9$ (PA = 96°), for Setup 3, and

² <http://www.iram.fr/IRAMFR/GILDAS>

Table 2. Coordinates of the protostars (see also Choi 2001; Di Francesco et al. 2001; López-Sepulcre et al. 2017; Maury et al. 2019) and the analyzed emission peaks (chosen from methanol and dimethyl ether emission, see text) in the outflows.

Position	$\alpha(2000)$	$\delta(2000)$
4A1	03 ^h 29 ^m 10 ^s .536	31° 13' 31".07
4A2	03 ^h 29 ^m 10 ^s .428	31° 13' 32".27
4B	03 ^h 29 ^m 12 ^s .000	31° 13' 08".10
4B'	03 ^h 29 ^m 12 ^s .813	31° 13' 06".97
SE peak	03 ^h 29 ^m 10 ^s .591	31° 13' 17".53
SW peak	03 ^h 29 ^m 10 ^s .061	31° 13' 18".61
North peak	03 ^h 29 ^m 10 ^s .966	31° 13' 47".87
As region	03 ^h 29 ^m 10 ^s .184	31° 13' 16".62

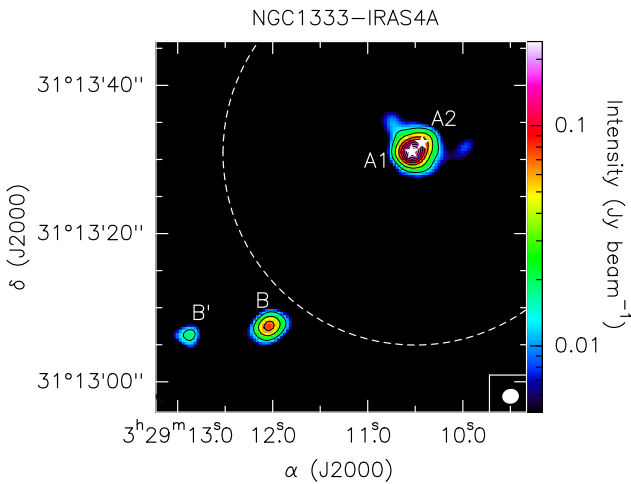


Fig. 2. Dust continuum emission maps of IRAS 4A at 95.85–99.45 GHz (Setup 3, see Table 1). Contours start at 3σ and increase by steps of 20σ , with $\sigma = 1.5 \text{ mJy beam}^{-1}$. The synthesized beam ($\sim 2''$) is represented in white in the lower right corner of the panel, the primary beam ($\sim 52''$) is shown with a dashed white circle. The millimeter continuum sources in the field are labeled following the nomenclature used by Choi (2001) for 4A1 and 4A2 and Di Francesco et al. (2001) for B and B'.

$4'.5 \times 3'.5$ (PA = 27°) for Setup 1. The half-power primary beam is $59'.2$ and $61'.4$ for Setup 3 and Setup 1, respectively.

4. Results

4.1. Dust continuum emission

Figure 2 shows the map of the dust continuum emission at 3 mm, whose emission peaks at the position of 4A1 and 4A2. As expected, the two sources are not disentangled as the angular resolution of $\sim 2''$ is too close to their angular separation ($\sim 1'.8$; Sect. 3). In addition, the two protostars IRAS 4B and IRAS 4B' were detected (e.g., Looney et al. 2000; Choi 2001; Di Francesco et al. 2001; Maury et al. 2019), even if they were located outside the primary beam of our observations ($\sim 52''$). The coordinates of all the four protostars are reported in Table 2.

The root mean square (RMS) noise level is $1.5 \text{ mJy beam}^{-1}$ and the peak flux toward IRAS 4A1+4A2 is $240 \pm 40 \text{ mJy beam}^{-1}$. Taking the error on the measured flux into account and considering the slightly different wavelength (2.7 mm) and angular resolution ($\sim 1'.2$) of the observations, this flux

value is consistent with the value found by López-Sepulcre et al. (2017). The uncertainties in the flux measurements include the amplitude calibration error ($\sim 15\%$) that dominates the RMS.

4.2. Line emission: maps

The present observations allow us to image both 4A1 and 4A2 and their molecular outflows. The study of the molecular content around the 4A1 and 4A2 protostars is beyond the scope of the present paper. Instead, we focus here on the molecular composition of the outflows.

Several lines from methanol (CH_3OH), acetaldehyde (CH_3CHO), dimethyl ether (CH_3OCH_3), and formamide (NH_2CHO) were detected along the outflows with a signal-to-noise ratio (S/N) higher than 3. Table 3 lists the detected lines with their spectroscopic properties. In Setup 3 we detected six lines of methanol that cover a range of upper level energy (E_{up}) from 7 to 28 K; eight lines of acetaldehyde with E_{up} between 13 and 23 K; and four lines of dimethyl ether, blended together and all with $E_{\text{up}} = 10 \text{ K}$. In Setup 1 we detected one line of formamide with E_{up} of 28 K.

Figure 1 shows the distribution of the line emission of the four detected iCOMs. To obtain the methanol map we integrated from -36 to 36 km s^{-1} with respect to the systematic velocity of the source ($\sim 6.5 \text{ km s}^{-1}$), for acetaldehyde between -15 to 15 km s^{-1} , while for formamide and dimethyl ether we integrated from -9 to 9 km s^{-1} . First, the methanol emission is extended ($\sim 1'$) and covers the lobes of the two outflows from the two protostars: north (North) and southwest (SW) lobes of the outflow from 4A2, and the southeast (SE) lobe from 4A1. Second, acetaldehyde emission is less extended than the methanol one ($\sim 15''$) and it is bright toward the southern lobes, especially toward the SE one. The dimethyl ether emission is not resolved being less than the beam size ($2''$) in two positions, in the North lobe and in the region As (named by Ceccarelli et al. 2017) where the SE and SW lobes seem to cross. Finally, formamide emission is also compact ($\sim 6''$) and is located around the As position (see also Ceccarelli et al. 2017). The same iCOMs are also detected in the central protostars (4A1+4A2); we note that the methanol and acetaldehyde emission is not visible in Fig. 1 because it is hidden by the dimethyl ether and formamide contours. Figure 1 clearly shows a first important result: the evidence of a spatial segregation between the different iCOMs due to the fact that their emission covers different outflow regions.

4.3. Line emission: spectra and intensities

In order to do a quantitative analysis, we extracted the spectra from different positions of the three lobes where both methanol and acetaldehyde emit. The first two selected positions correspond to the emission peaks of methanol in the two southern lobes, SE and SW, while the last selected position corresponds to the emission peak of dimethyl ether in the northern lobe, North (Fig. 1). A fourth position is the one where formamide and dimethyl ether emit, called As. The spectra extracted at the pixels corresponding to the four positions are shown in Fig. 3. It is immediately evident that the SE position is richer and brighter in iCOMs when compared to the others (SW, North, and As).

We then derived the velocity-integrated line intensities of each detected transition using a Gaussian fit, obtained with the CLASS package of the GILDAS software. All the lines used for the analysis are not contaminated by other species and are well isolated. For instance, three of the six detected methanol lines, namely $2_{-1,2}-1_{-1,1}$ E ($E_{\text{up}} = 13 \text{ K}$), $2_{0,2}-1_{0,1}$ A ($E_{\text{up}} = 7 \text{ K}$), and

Table 3. Spectral parameters and fit results of the detected iCOM emission lines observed using the NOEMA WideX backend toward the IRAS 4A outflow peaks (see text and Table 2).

Transition	Spectral parameters			Outflow SE			Outflow SW			Outflow North			Region As ^(a)		
	Frequency ^(b) [GHz]	E_{up} ^(b) [K]	$\log A_{ij}$ ^(b)	Area ^(c) [K km s ⁻¹]	T_{peak} [K]	RMS ^(d) [mK]	Area ^(c) [K km s ⁻¹]	T_{peak} [K]	RMS ^(d) [mK]	Area ^(c) [K km s ⁻¹]	T_{peak} [K]	RMS ^(d) [mK]	Area ^(c) [K km s ⁻¹]	T_{peak} [K]	RMS ^(d) [mK]
CH ₃ OH															
2 _{1,2} -1 _{1,1} A	95.91431	21.4	-5.6	17.1(0.9)	1.4	20	2.7(0.3)	0.4	20	5.1(0.5)	0.4	20	≤0.5	≤0.05	30
2 _{-1,2} -1 _{-1,1} E ^(e)	96.73936	12.5	-4.6												
2 _{0,2} -1 _{0,1} A ^(e)	96.74138	6.9	-5.6	199 (4)	12	20	69(4)	5	30	48(4)	3	20	37(1)	2.5	30
2 _{0,2} -1 _{0,1} E ^(e)	96.74454	20.1	-5.5												
2 _{1,1} -1 _{1,0} E	96.75550	28.0	-5.5	11.2(0.3)	0.9	20	2.0(0.2)	0.3	30	3.2(0.3)	0.2	20			
2 _{1,1} -1 _{1,0} A	97.58280	21.6	-5.6	21.5(0.2)	1.9	20	2.5(0.3)	0.3	30	4.4(0.3)	0.4	30	≤0.5	≤0.05	30
CH ₃ CHO															
5 _{0,5} -4 _{0,4} E	95.94744	13.9	-4.5	3.9(0.2)	0.4	20	≤0.6	≤0.06	20	0.8(0.4)	0.1	20	≤0.5	≤0.05	30
5 _{0,5} -4 _{0,4} A	95.96346	13.8	-4.5	3.7(0.3)	0.4	20	1.7(0.4)	0.1	20	1.3(0.5)	0.1	20	≤0.5	≤0.05	30
5 _{2,4} -4 _{2,3} A	96.27425	22.9	-4.6	1.1(0.4)	0.1	30	0.7(0.3)	0.07	20	1.0(0.2)	0.1	30	0.5(0.3)	0.1	20
5 _{2,4} -4 _{2,3} E	96.42561	22.9	-4.6	1.1(0.2)	0.2	30	≤0.7	≤0.07	20	0.8(0.3)	0.06	30	≤0.3	≤0.03	20
5 _{2,3} -4 _{2,2} E	96.47552	23.0	-4.6	0.8(0.2)	0.1	20	≤0.7	≤0.07	20	≤0.8	≤0.08	30	≤0.3	≤0.03	20
5 _{2,3} -4 _{2,2} A	96.63266	23.0	-4.6	1.5(0.3)	0.1	20	≤0.7	≤0.07	20	≤0.8	≤0.08	30	≤0.3	≤0.03	20
5 _{1,4} -4 _{1,3} E	98.86331	16.7	-4.5	2.3(0.4)	0.2	20	1.6(0.8)	0.1	20	2.1(0.5)	0.2	30	2.8(0.6)	0.1	20
5 _{1,4} -4 _{1,3} A	98.90094	16.5	-4.5	2.5(0.5)	0.2	20	≤0.6	≤0.06	20	1.9(0.3)	0.2	30	2.0 (0.3)	0.1	20
CH ₃ OCH ₃															
4 _{1,4} -3 _{0,3} EA ^(e)	99.32443	10.2	-5.3												
4 _{1,4} -3 _{0,3} AE ^(e)	99.32443	10.2	-5.3	≤0.2	≤0.02	15	≤0.3	≤0.03	15	2.1(0.3)	0.12	15	1.8(0.5)	0.09	15
4 _{1,4} -3 _{0,3} EE ^(e)	99.32521	10.2	-5.3												
4 _{1,4} -3 _{0,3} AA ^(e)	99.32607	10.2	-5.3												
NH ₂ CHO ^(f)															
4 _{1,4} -3 _{1,3}	81.69354	12.8	-4.5	≤0.2	≤0.02	7	≤0.1	≤0.01	7	≤0.06	≤0.006	7	0.4(0.1)	0.04	10

Notes. ^(a)Region where formamide and dimethyl ether emits (Ceccarelli et al. 2017). ^(b)Frequencies and spectroscopic parameters are retrieved from the JPL (Jet Propulsion Laboratory; Pickett et al. 1998) molecular database and from the CDMS (Cologne Database for Molecular Spectroscopy; Müller et al. 2005): for CH₃OH by Xu et al. (2008), for CH₃CHO by Kleiner et al. (1996), for CH₃CHO₃ by Neustock et al. (1990), for NH₂CHO by Kirchhoff et al. (1973). Upper level energies refer to the ground state of each symmetry. ^(c)Mean velocity-integrated line flux over the whole velocity emission range from the spectra extracted at the CH₃CHO and CH₃OH transitions at each outflow peaks (see Table 2). In case of non-detection we report the 3 σ limit. The lines are centered at ~ 3 km s⁻¹, ~ 1 km s⁻¹, ~ 11 km s⁻¹ for outflow SE, SW and North respectively, in agreement with the expected outflow velocity (Santangelo et al. 2015) given the WideX channel resolution (~ 6 km s⁻¹). ^(d)The rms is computed over a 200 km s⁻¹ band around each line. ^(e)These lines are blended together at the WideX resolution (~ 2 MHz), therefore they are not used for the non-LTE analysis. ^(f)From Setup 1.

2_{0,2}-1_{0,1} E ($E_{up} = 21$ K), are blended together at the WideX resolution (~ 2 MHz); therefore, they were not used in the analysis described in the next section. Table 3 reports the fit results; in the case of non-detection, the 3 σ limit is reported.

5. Derivation of the column densities and abundance ratios

5.1. Methanol and acetaldehyde

We used the detected lines of methanol and acetaldehyde to estimate their column densities in the four positions of Table 2. We used the standard rotational diagram method (Goldsmith & Langer 1999), which assumes local thermodynamic equilibrium (LTE) and optically thin line emission. We checked a posteriori that the latter assumption is valid. Also, because the map in Fig. 1 shows that the emission is more extended with respect to the observation beam, we did not apply a dilution factor. The used error bar of each data point includes the spectral RMS and the calibration error ($\sim 15\%$).

Figure 4 shows the rotational diagrams of methanol and acetaldehyde in the SE, SW, and North positions (Table 2), and Table 4 lists the fitted values. In the As position, we could not build a rotational diagram for either of the two species as not enough lines were detected. In this case we obtained an estimate of their column density by assuming a rotational temperature ranging from 10 to 30 K, a range that includes the temperatures found in the other positions (SE, SW, and North). If no line was detected we used the 3 σ limit.

To compute the methanol over acetaldehyde abundance ratios, quoted in Table 4, we adopted the assumptions that the lines emitted by the two species come from the same region, and therefore possess the same rotational temperature T_{rot} . Under these two assumptions the column density ratio R of the two species is obtained by taking the column density N_x of each species at the same rotational temperature T_{rot} , namely $R = N_1(T_{rot})/N_2(T_{rot})$. The error bar δR is then obtained by computing R at the smallest and largest T_{rot} of the two species. For example, in the Outflow SE the derived T_{rot} is equal to (11 ± 3) K and (9 ± 2) K in methanol and acetaldehyde, respectively;

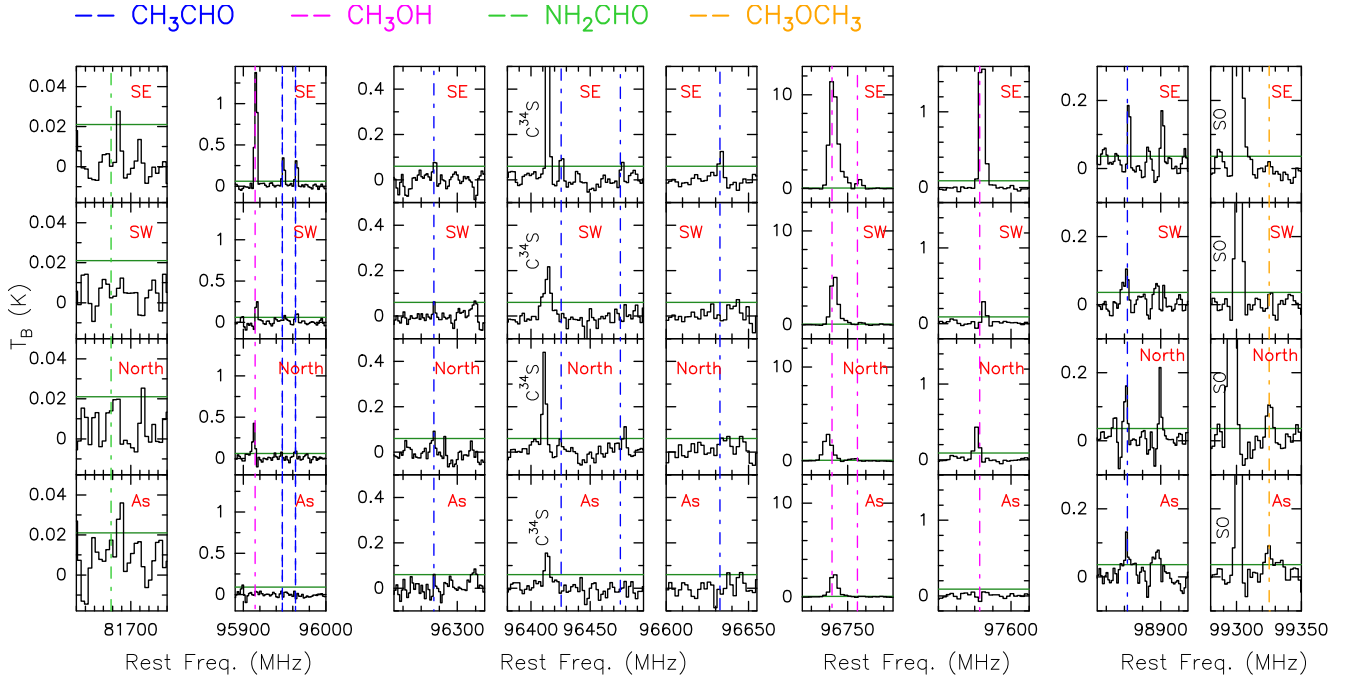


Fig. 3. Spectra toward the four positions along the outflows of IRAS 4A listed in Table 2. The horizontal green lines represent the 3σ levels (reported in Table 3); the vertical dashed lines in blue and magenta represent the rest frequency of acetaldehyde and methanol lines, respectively. The rest frequency corresponds to the protostar Local Standard of Rest (LSR) velocity (6.5 km s^{-1}).

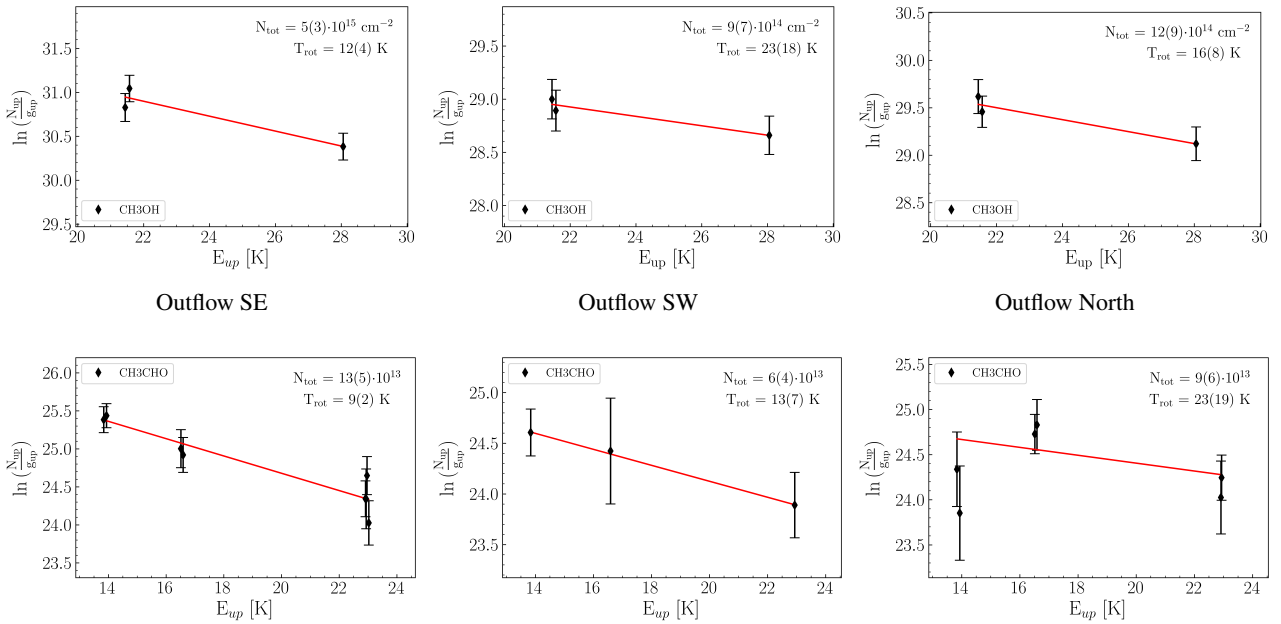


Fig. 4. *Upper panels:* rotational diagrams of methanol (CH_3OH) in outflow SE, SW, and North (from left to right). *Lower panels:* rotational diagrams of acetaldehyde (CH_3CHO) in outflow SE, SW, and North. The parameters N_{up} , g_{up} , and E_{up} are the column density, the degeneracy, and the energy of the upper level. The error bars on $\ln(N_{\text{up}}/g_{\text{up}})$ are computed by taking the calibration error on the integrated flux (15%) into account. The red lines represent the best fits.

therefore, to estimate the error δR we computed $R(T_{\text{rot}})$ at 7 and 14 K. We note that the method described above allows us to reduce the error bar in the abundance ratio because the calibration uncertainty, which enters in the column density estimate of each species, cancels out when considering the column density of two species derived with the same observation data set.

For methanol, we obtain a column density $N_{\text{CH}_3\text{OH}} \simeq 9 - 50 \times 10^{14} \text{ cm}^{-2}$ and a rotational temperature $T_{\text{CH}_3\text{OH}}$ between 11

and 23 K. For acetaldehyde, we obtain $N_{\text{CH}_3\text{CHO}} \simeq 0.6 - 1.3 \times 10^{14} \text{ cm}^{-2}$ and $T_{\text{CH}_3\text{CHO}}$ between 9 and 23 K. Their abundance ratios vary from 10–20 to ~ 44 in the three lobes; more precisely, the SE lobe is the one with the largest $\text{CH}_3\text{OH}/\text{CH}_3\text{CHO}$ abundance ratio. In As we only derive a lower limit to the $\text{CH}_3\text{OH}/\text{CH}_3\text{CHO}$ abundance ratio of ≥ 20 . We note that our observations provide different values of the $\text{CH}_3\text{OH}/\text{CH}_3\text{CHO}$ abundance ratio compared to those previously derived by

Table 4. Results of the LTE analysis with the rotational diagrams for each outflow peak, using the observation with the NOEMA WideX backend.

Molecule		Outflow SE	Outflow SW	Outflow North	Region As ^(a)	L1157-B1 ^(b)
CH ₃ OH	N_{tot} [10 ¹⁴ cm ⁻²]	50(30)	9(7)	12(9)	5-15	130(30)
	T_{rot} [K]	11(3)	23(18)	18(8)	10-30 ^(c)	10.0(1.1)
CH ₃ CHO	N_{tot} [10 ¹⁴ cm ⁻²]	1.3(0.5)	0.6(0.4)	0.9(0.6)	≤(0.25-0.5)	0.7(0.3)
	T_{rot} [K]	9(2)	13(7)	23(19)	10-30 ^(c)	8(1)
CH ₃ OCH ₃	N_{tot} [10 ¹⁴ cm ⁻²]	≤0.5	≤0.7	1.6(0.7)	1.0(0.4)	3
	T_{rot} [K]	11	16	19	10-30 ^(c)	9
NH ₂ CHO	N_{tot} [10 ¹⁴ cm ⁻²]	≤0.02	≤0.02	≤0.02	0.03(0.02)	–
	T_{rot} [K]	11	16	19	10-30 ^(c)	–
$\frac{\text{CH}_3\text{OH}}{\text{CH}_3\text{CHO}}$ ^(d)		44(5)	11(3)	17(3)	≥20	190(60)

Notes. In the last row are shown the values of the abundance ratio of methanol to acetaldehyde for each outflow peak. ^(a)Region where formamide and dimethyl ether emit (Ceccarelli et al. 2017). ^(b)From Codella et al. (2020) based on interferometric observations. ^(c)Fixed rotational temperature used to derive a range of possible N_{tot} . ^(d)Abundance ratio computed dividing the best fit column densities derived assuming that the two species are tracing the same gas with the same properties (see text).

Holdship et al. (2019, ~300) toward the south and north lobes of the IRAS 4A outflows via single-dish observations. We attribute this difference to the fact that the single-dish observations of IRAS 4A by Holdship et al. (2019) include emission from a much larger region (including some from the central protostars) with respect to that probed by the present SOLIS observations. Moreover Holdship et al. (2019) do not explicitly derive the emitting size, even though they minimize with respect to this parameter; since the maximization is done independently for each species, their column density ratio has a relatively large intrinsic uncertainty. Therefore, the interferometric images allow us to minimize the risk of mixing different gas components (typical of shocked regions).

The abundance ratio analysis confirms what we can see from the emission maps (Fig. 1), namely that the methanol and acetaldehyde emission (and their relative abundance) is quite different in the SE lobe with respect to the SW and North lobes. We note that the difference cannot be attributed to excitation effects, having the methanol and acetaldehyde lines with similar upper level energies (E_{up} from 7 to 28 K), similar Einstein coefficients ($A_{ij} \sim 10^{-5} \text{ s}^{-1}$), and comparable derived temperatures, within the measurement errors.

To summarize, the SW and North lobes have a relatively low CH₃OH/CH₃CHO abundance ratio (8–20), whereas the SE lobe presents a ratio at least two times higher (~44). Since the SW and North lobes belong to the same outflow emanating from 4A2 and the SE lobe traces the outflow emanating from 4A1, it seems reasonable to attribute the observed difference to an intrinsic difference in the two outflows. We explore this hypothesis in the next section with the help of an astrochemical model.

5.2. Dimethyl ether and formamide

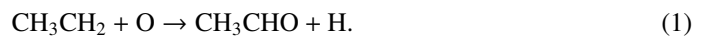
Regarding formamide and dimethyl ether, we detected only one line at most of the latter and four lines (blended at the WideX resolution, ~2 MHz) of the former in any position (see Table 3). For this reason, we did not carry out the rotational diagram analysis as we did for the other iCOMs. Furthermore, while formamide is marginally resolved at the As position, dimethyl ether is not resolved in any outflow peaks (see Fig. 1). If detected, we derived the column densities using the integrated area of the

4_{1,4}–3_{1,3} line for formamide and the blended ones for dimethyl ether, assuming fixed rotational temperatures. As for methanol and acetaldehyde, we used 11, 16, and 19 K for SE, SW, and North, respectively, and 10–30 for As. If not detected, an upper limit on the column density is derived considering the 3 σ limit of the spectra and using the above rotational temperatures. The derived values are reported in Table 4.

6. Astrochemical modeling

We ran our model GRAINOBLE+ in order to reproduce the observations and understand what could be the cause of the observed difference in the CH₃OH/CH₃CHO abundance ratio in the different lobes of the IRAS 4A outflows.

There is solid evidence (observational, theoretical, and experimental) that methanol is synthesized on the grain surfaces via the hydrogenation of iced CO by the successive addition of H atoms (Boogert et al. 2015; Tielens & Hagen 1982; Watanabe & Kouchi 2002). On the contrary, the acetaldehyde formation route is less clear, and the two paths, formation in the gas phase or on the grain surfaces, are still debated. Specifically, grain surface models predict that CH₃CHO could be formed through the combination of the two radicals CH₃ and HCO (previously formed by photodissociation of methanol and formaldehyde, respectively) on the surface of the grains (Garrod & Herbst 2006). However, recent quantum chemistry computation by Enrique-Romero et al. (2016, 2019) show that alternative channels leading back to the two simple species CH₄ and CO are competitive. Conversely, the gas-phase models claims that acetaldehyde formation could occur by the oxidation of hydrocarbons (formed previously on the grain mantles via hydrogenation of carbon chains; Charnley et al. 1992; Charnley 2004). In particular, the injection from grain mantles of ethane (C₂H₆) is expected to drive CH₃CH₂ that will then react in the gas phase with atomic oxygen, giving CH₃CHO (Charnley 2004). The crucial reaction is therefore



Following these two possibilities, we ran a grid of astrochemical models in order to reproduce our observations and to understand the possible cause of the difference in the observed CH₃OH/CH₃CHO values in the two IRAS 4A outflows.

6.1. Model description

GRAINOBLE+ is a gas-grain model simulating the chemical evolution of gas and ices. It is the upgraded version of GRAINOBLE, initially developed by Taquet et al. (2012a); in particular, it is re-coded and improved in terms of computational efficiency and treatment of processes. The GRAINOBLE+ version³ allows an easy incorporation of many complicated processes that occur in the gas and on the grain surfaces. The code can carry out an easy implementation of evolution of physical conditions of a cloud with a given time-dependent physical profile. Additionally, the new code allows a distribution of size for the grains, multi-layer formation of the grain ice mantle, growth and depletion of the ice, and desorption.

In this work we used a chemical network of 522 species and 7785 reactions based on the KIDA database⁴, which has been updated from various recent works (e.g., Loison et al. 2014; Balucani et al. 2015; Skouteris et al. 2017, 2018).

In order to simulate the passage of a shock in IRAS 4A, we employed the gas-phase mode of GRAINOBLE+. The simulation follows two steps: (1) a cold molecular gas phase at 10 K and $2 \times 10^4 \text{ cm}^{-3}$ H-nuclei density (n_{H}); (2) a post-shock gas phase where density and temperature suddenly jump to $2 \times 10^6 \text{ cm}^{-3}$ and 70 K. In other words, the second phase inherits the evolved chemical composition of the cloud from the cold phase⁵. Additionally, the gas is infused by species that were formerly synthesized in ice mantles due to the grain sputtering caused by the shock passage.

It is possible that before reaching the temperature of 70 K, the shocked gas passes through a short initial phase with high temperature. However, this phase unlikely affects the results reported in the next section because there are no known gas-phase reactions with activation barriers that form acetaldehyde. This is confirmed by models taking into account the temperature evolution in the shocked gas (e.g., Nesterenok 2018; Burkhardt et al. 2019).

We do not have precise estimates of the density and temperature in the positions where we derived the $\text{CH}_3\text{OH}/\text{CH}_3\text{CHO}$ abundance ratio. However, the values derived at positions close to those selected here via a non-LTE analysis of observed SO_2 lines (Taquet et al. 2020) are similar to those adopted in our modeling. We assumed that the cosmic ray ionization rate is the same as toward L1157-B1 ($\zeta = 3 \times 10^{-16} \text{ s}^{-1}$; Podio et al. 2014) and that the abundance of the injected species are also similar to the values adopted for L1157-B1 (see Table B1 of Codella et al. 2017), listed in Table 5.

We ran series of models to compare the observed $\text{CH}_3\text{OH}/\text{CH}_3\text{CHO}$ abundance ratio with the predicted ratio, and to understand what the ratio depends on. We start exploring the gas-phase formation route of acetaldehyde assuming that its formation is dominated by reaction (1) in the passage of shock. Oxygen is much more abundant than the injected ethyl radical in the post-shock phase; therefore, CH_3CH_2 is the bottleneck of the rate of the reaction (1).

First, we ran a grid of 169 models with different injected abundances at the beginning of the shocked phase for ethyl radical (CH_3CH_2) and methanol in the ranges $[4 \times 10^{-9}, 4 \times 10^{-7}]$ and $[4 \times 10^{-8}, 4 \times 10^{-6}]$, respectively. The methanol abundance range was chosen in order to include the observed values in the

Table 5. Injected abundances (with respect to H-nuclei) into the gas phase at the second step of the model.

Molecules	Injected abundances (/H)
CO_2	3×10^{-5}
H_2O	2×10^{-4}
OCS	2×10^{-6}
H_2CO	1×10^{-6}
NH_3	2×10^{-5}

Notes. These values are based on previous observations toward L1157-B1 (Codella et al. 2017).

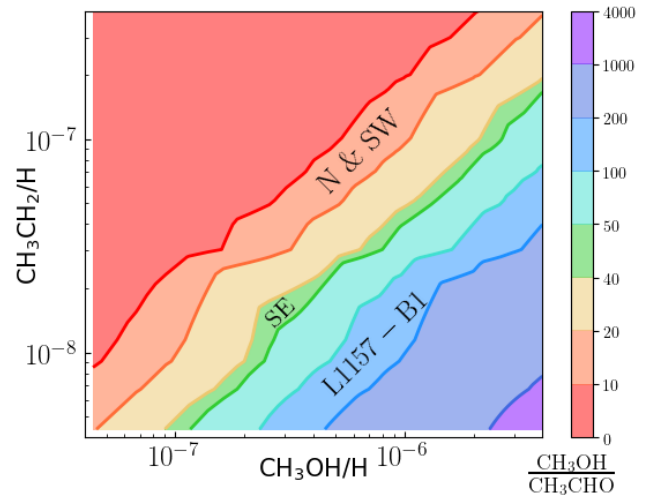


Fig. 5. Contour map of the $\text{CH}_3\text{OH}/\text{CH}_3\text{CHO}$ abundance ratio at 1000 yr after the start of the shock passage. The x - and y -axis are the injected abundances of methanol [$4 \times 10^{-8}, 4 \times 10^{-6}$] and the parent molecule of acetaldehyde, ethyl radical CH_3CH_2 [$4 \times 10^{-9}, 4 \times 10^{-7}$], respectively. The measured methanol to acetaldehyde abundance ratio of the North and SW outflows (8–20) fall in the orange band, and that of SE (38–50) in the green band; the L1157-B1 value (130–250) is covered by the blue band (Codella et al. 2020).

hot corinos and in the protostellar shocks (the L1157-B1 outflow in particular); the ethyl radical range was chosen in order to match our observed $\text{CH}_3\text{OH}/\text{CH}_3\text{CHO}$ abundance ratio. The results are shown in Fig. 5 and described in the next section.

Second, we studied the influence of the density and cosmic ray ionization rate ζ on the chemical evolution, and how the CH_3OH and CH_3CHO abundances and their relative ratio depend on the time after the shock passage. We note that protostellar shocks could be local accelerators of cosmic ray protons (Padovani et al. 2016), and therefore in this work ζ is an unknown parameter. We then ran two additional models. In the first we decrease the chosen n_{H} density value to $2 \times 10^5 \text{ cm}^{-3}$; in the second we decrease the chosen cosmic ray ionization rate value to $\zeta = 3 \times 10^{-17} \text{ s}^{-1}$ for the post-shock phase. The injected abundances of methanol is 3×10^{-6} and for the ethyl radical it is 3×10^{-7} in both cases. These values are chosen such that the models reproduce the observed $\text{CH}_3\text{OH}/\text{CH}_3\text{CHO}$ abundance ratios for the SW and North lobes (8–20) at 1000 yr (orange band in Fig. 5) and for the SE lobe as well. The results are shown in Fig. 6 and described in the next section.

Finally, we ran a model with the assumption that acetaldehyde is synthesized on the ice mantles and injected directly into the gas phase at the passage of the shock.

³ A detailed description of the GRAINOBLE+ model will be presented in a forthcoming dedicated article.

⁴ <http://kida.obs.u-bordeaux1.fr>

⁵ We do not compute the grain mantle composition as it is treated as a parameter in the following analysis.

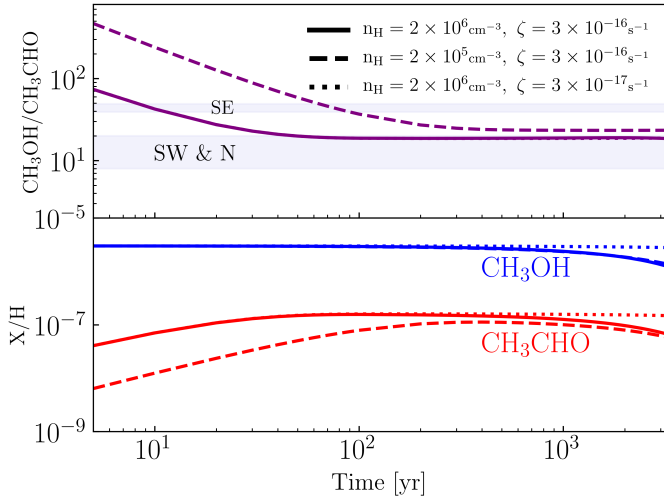


Fig. 6. Time evolution of abundances of methanol in blue and acetaldehyde in red (*bottom*) and their ratios in purple (*top*) for the same injected methanol abundance, 3×10^{-6} , and ethyl radical value, 3×10^{-7} . The different line styles correspond to models run with different conditions, as reported in the upper panel legend. The $\text{CH}_3\text{OH}/\text{CH}_3\text{CHO}$ abundance ratio is constant if both species are directly injected from the grain mantles (see text).

6.2. Model results

Figure 5 shows the contour map of the $\text{CH}_3\text{OH}/\text{CH}_3\text{CHO}$ abundance ratio at 1000 yr after the shock passage as a function of the injected methanol and ethyl radical, assuming that acetaldehyde is entirely synthesized in the gas phase. We note that the chosen age (1000 yr) is approximately the same magnitude as the kinematical age of L1157-B1 (Podio et al. 2016; Codella et al. 2017) and, likely, IRAS 4A outflows. First, the figure shows that there is a linear dependence of the $\text{CH}_3\text{OH}/\text{CH}_3\text{CHO}$ abundance ratio on the injected methanol abundance and on the ethyl radical abundance in the range explored in our simulations. Second, reasonable values of methanol and ethyl radical abundance can reproduce the observed values in the four IRAS 4A outflow positions that we studied (Table 2).

In Fig. 6, we show the evolution of methanol and acetaldehyde abundance as a function of the time after the shock passage, for different densities n_{H} and cosmic ray ionization rates ζ . Given that methanol is a grain surface product, even by varying n_{H} or ζ , the injected abundance remains constant in the early stages of the shock up to $\sim 2 \times 10^3$ yr. The time evolution of acetaldehyde in the early stages is different from that of methanol; while the latter remains constant, acetaldehyde abundance increases soon after the shock passage. This is expected since we assumed that acetaldehyde is a gas phase product and its evolution is dominated by the formation through ethyl radical reaction (1). Furthermore, the time evolution of acetaldehyde in the post-shock phase is influenced by variation of n_{H} or ζ . Lower density slows down the formation rate of acetaldehyde in the early stages; this is due the fact that in lower density gas the ion abundance is higher. Therefore, the contribution of destruction rates is higher in the evolution. Similar to methanol, a lower cosmic ray ionization rate does not affect the early stages.

Finally, we ran a model in which acetaldehyde is synthesized on the icy dust surfaces and injected directly into the gas phase. Therefore, in the model the species injected into the gas phase right after the shock is no longer the ethyl radical but acetaldehyde, whose abundance is chosen to be equal to the

observed one. Therefore, the gas-phase production of acetaldehyde is, in this case, negligible. As for methanol, the abundance of acetaldehyde, now injected from grains, remains constant up to $\sim 2 \times 10^3$ yr when the destruction by ions (H_3O^+ in this specific case) becomes dominant. Therefore, the difference in the abundance of acetaldehyde between the gas- and grain-synthesized models is only within the first 200 yr of the shocked phase, when acetaldehyde takes time to be formed by the reactions between ethyl radical with atomic oxygen.

7. Discussion

7.1. Two IRAS 4A outflows

Our new SOLIS observations show that the two outflows emanating from 4A1 and 4A2, previously identified by Choi (2005) and Santangelo et al. (2015) via simple molecules (SiO, CO, and SO), are enriched with methanol all across the three (visible) lobes. Conversely, acetaldehyde is spread only over the southern lobes and is concentrated in a compact spot in the northern one. Therefore, a first conclusion of this work is that in the protostellar post-shock regions there is the release in gas phase of methanol, previously formed on the grain surfaces, and the production of acetaldehyde. The statistics are very poor for the moment, with the two IRAS 4A outflows and the L1157-B1 outflow in which acetaldehyde is detected with interferometric observations (Codella et al. 2015, 2017, 2020).

For the IRAS 4A outflows, the SE lobe is richer in both methanol and acetaldehyde, specifically the outflow emanating from 4A1. We note that this is the opposite behavior with respect to the SiO emission, which is instead brighter along the 4A2 outflow (Choi 2005). This anti-correlation with SiO is also seen in other (simple) molecules, such as NH_3 , H_2CO , and HCN by Choi et al. (2011). As Choi et al. (2011) suggested, it could be due to a different strength of the shock (the sputtering of Si could require different shock velocities with respect to the other molecules) or to SiO tracing different physical conditions with respect to the other molecules. For example, SiO could trace the jet, while the other molecules could have originated in the gas entrained by the jet (e.g., Bachiller et al. 1998; Ospina-Zamudio et al. 2018, 2019). Linked with this, the different spatial distribution between SiO and other species, could be due to time-evolution effects, namely different ages of the shocks, as previously observed in other outflows (e.g., Castets et al. 2001). We discuss this point further in the next section.

Finally, the origin of the iCOMs emission in the As position is not clear. It does not seem to be clearly associated with any of the two southern lobes, but rather with the point where they intersect. That would imply that additional shocks can occur at the interface of the swept-up cavities opened up by the jets. Higher spatial resolution observations are needed to confirm or reject this hypothesis.

7.2. $\text{CH}_3\text{OH}/\text{CH}_3\text{CHO}$ abundance in IRAS 4A1 and 4A2 outflows

In Sect. 5 we measured the methanol to acetaldehyde abundance ratio toward the three positions of the two IRAS 4A outflows, in the North, SW, and SE lobes (Table 4). While the North and SW lobes have a similar values, between 8 and 20 (considering the error bars), the SE lobe has higher $\text{CH}_3\text{OH}/\text{CH}_3\text{CHO}$, 38–50. In other words, the methanol to acetaldehyde abundance ratio is about two times higher in the outflow emanating from 4A1 with respect to that from 4A2. In this section we try to understand the

origin of this difference, keeping in mind that while methanol is a past grain-surface product, acetaldehyde can either be itself a past grain-surface or a gas-phase product.

One easy possible explanation then of the $\text{CH}_3\text{OH}/\text{CH}_3\text{CHO}$ difference is that the grain mantle composition is different in the two outflows. However, this seems unlikely because, on the one hand, no gradient in the ratio is seen between the North and SW lobes of the 4A2 outflow; moreover, the SW and SE lobes are very close in space, closer than the two 4A2 outflow positions where we estimated the $\text{CH}_3\text{OH}/\text{CH}_3\text{CHO}$ abundance ratio. Therefore, although we cannot totally exclude it, it seems to us that the different grain composition is an improbable explanation.

If acetaldehyde is synthesized by the gas-phase reaction (1), there are more possibilities than a different grain mantle composition. As shown by the modeling in Sect. 6, a lower density or a younger age of the 4A1 outflow with respect to 4A2 would explain the observed $\text{CH}_3\text{OH}/\text{CH}_3\text{CHO}$ difference. Specifically, if the two outflows are very young and 4A1 is younger than about 200 yr, then this would explain why its ratio is higher than the 4A2 value (see Fig. 6).

Unfortunately, our observations did not have enough methanol lines to allow a meaningful non-LTE analysis to derive the volume density, so we do not know if the density in the 4A1 outflow is lower than in the 4A2 outflow. With a non-LTE analysis on SO_2 , Taquet et al. (2020) suggest that there is no significant difference in density between the outflow driven by 4A1 and that from 4A2. On the other hand, assuming a typical shock velocity of 100 km s^{-1} , we estimate a kinematical age of ~ 200 yr for the 4A1 outflow which has a very short extent; this seems to support the younger age of 4A1 hypothesis. Furthermore, Santangelo et al. (2015), using high spatial resolution observations of CO, SiO, and SO, showed that the 4A1 jet is faster than the 4A2 one; this, combined with the smaller spatial extension again supports the hypothesis that the 4A1 outflow is younger than that of 4A2. In favor of a different age for the two outflows there is also the observed chemical differentiation between the two driving sources: 4A1 is bright in the continuum but lacks iCOM line emission, exactly the opposite of 4A2 (e.g., López-Sepulcre et al. 2017). One of the possible explanations for this situation is the smaller hot corino size, which could also imply a younger age of 4A1, and this agrees with the younger age of its outflow as well.

In summary, the different $\text{CH}_3\text{OH}/\text{CH}_3\text{CHO}$ abundance ratio measured in the 4A1 and 4A2 outflows is unlikely caused by a different grain mantle composition of the two outflows because the more extended 4A2 outflow shows no significant variation in this ratio on a scale of about 6000 au. On the contrary, the observed $\text{CH}_3\text{OH}/\text{CH}_3\text{CHO}$ abundance ratio is consistent with the scenario in which (i) the 4A1 outflow is younger (and consequently faster) than the 4A2 outflow and (ii) in both outflows acetaldehyde is synthesized in the gas phase. The major reaction is between atomic oxygen and ethyl radical. The gas-phase synthesis hypothesis also agrees with theoretical quantum chemistry studies (Enrique-Romero et al. 2016, 2019). Thus, although terrestrial laboratory experiments show that acetaldehyde can be formed on the surfaces of dust grains (e.g., Bennett et al. 2005a,b; Öberg et al. 2009), our results provide evidence that the gas-phase formation route cannot be neglected, and actually appears to be the dominant process in the IRAS 4A outflows. We note that these conclusions are robust as they depend very little on the details of the modeling being based on known reactions in the gas phase.

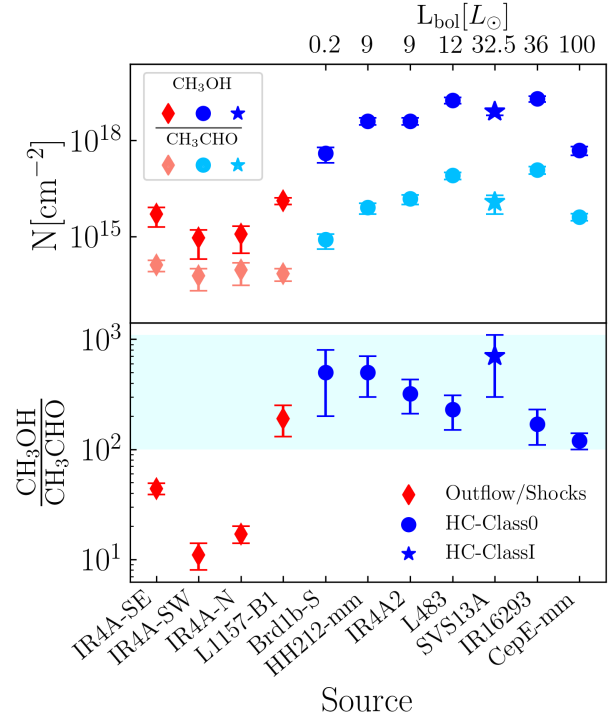


Fig. 7. Abundance ratios of CH_3OH to CH_3CHO (bottom panel) and the CH_3OH and CH_3CHO column density (upper panel) compared to different sources whose emitting size has been estimated via interferometric observations: the values in the outflows of IRAS 4A (this paper), in the outflow of L1157-B1 (Codella et al. 2020), the Class I source SVS 13A (Bianchi et al. 2019), and the Class 0 sources, in decreasing order of bolometric luminosity: Barnard 1b-S (Marcelino et al. 2018), HH212-mm (Bianchi et al. 2017; Codella et al. 2020), IRAS 4A2 (Taquet et al. 2015; López-Sepulcre et al. 2017), L483 (Jacobsen et al. 2019), IRAS 16293-2422B (Jørgensen et al. 2016), CepE-mm (Ospina-Zamudio et al. 2018). The outflow values are shown in red (pink for CH_3CHO), the hot corinos in blue (cyan for CH_3CHO), using diamonds for the outflows, dots for Class 0 sources, and stars for the Class I sources. The cyan band represents the area in which the hot corino values fall.

7.3. Comparison with other solar-type objects

Figure 7 shows the methanol to acetaldehyde abundance ratio in the IRAS 4A outflows, compared with the values measured in other low and intermediate star forming regions for which the emitting size as been estimated via interferometric observations: the L1157-B1 molecular shock and seven hot corinos.

First, the IRAS 4A outflows have a much lower value for $\text{CH}_3\text{OH}/\text{CH}_3\text{CHO}$ with respect to the L1157-B1 value (130–250), reliably measured by Codella et al. (2020). Following the discussion of the previous section, this could be due to a difference in the composition of the grain mantles, to a lower density, or to a younger age of the 4A outflows with respect to the L1157-B1 value. At present, we do not have enough information to support or rule out any of the three possibilities; a more accurate analysis of the IRAS 4A outflows is needed. Obviously, having more information of one key actor, the abundance of ethyl radical in these outflows, could shed more light on why the two outflow systems are different.

Finally, the same difference observed between the IRAS 4A and L1157 outflows, if not larger, is observed with respect to the values measured in Class 0 and I hot corinos (Marcelino et al. 2018; Bianchi et al. 2017, 2019; Taquet et al. 2015; López-Sepulcre et al. 2017; Jacobsen et al. 2019; Jørgensen et al. 2016; Codella et al. 2020; Ospina-Zamudio et al. 2018).

In Fig. 7, we ordered the hot corinos according to their increasing bolometric luminosity L_{bol} , keeping in mind that the measure of L_{bol} is relatively uncertain. It is possible to note an interesting trend: in the Class 0 hot corinos, the $\text{CH}_3\text{OH}/\text{CH}_3\text{CHO}$ abundance ratio decreases with increasing L_{bol} . Our modeling (Sect. 6) is not directly applicable to the hot corino case for two main reasons: 1) the hot corino density ($n_{\text{H}} \sim 10^7 \text{ cm}^{-3}$) is higher than those used in our model (Figs. 6 and 2) there is continuous injection of the infalling material toward the center. Having said that, it seems improbable that the behavior shown in Fig. 7 has something to do with a time effect. In the hot corino conditions (higher density and low cosmic ionization rate) the synthesis in the gas phase is fast during the first decades, while the destruction by molecular ions is slow in the later stages ($\geq 10^5$ yr), leading to a $\text{CH}_3\text{OH}/\text{CH}_3\text{CHO}$ abundance ratio that is almost constant.

On the contrary, a possible interpretation is that higher luminosity corresponds to larger hot corino sizes (namely larger regions with a dust temperature ≥ 100 K; Ceccarelli et al. 2007) and, assuming a central peaked density distribution, regions with lower densities. Since methanol is produced during the pre-stellar phase by hydrogenation of frozen CO (Taquet et al. 2012b; Vasyunin et al. 2017), a higher density will bring a greater methanol abundance; acetaldehyde, on the other hand, could be either a past grain-surface or a present-day gas-phase product (see Sect. 6). Therefore, the decreasing $\text{CH}_3\text{OH}/\text{CH}_3\text{CHO}$ abundance ratio could indicate that while methanol abundance decreases with density, acetaldehyde or its gas-phase precursors do not. We note that these conclusions have to be taken with caution as the errors on the hot corinos bolometric luminosity are relatively large, but they are worth a deeper study.

8. Conclusions

In this work we reported new observations using the IRAM/NOEMA interferometer in the context of the SOLIS Large Program, and the detection of several iCOMs in the two outflows emanating from IRAS 4A1 and 4A2: methanol, acetaldehyde, dimethyl ether, and formamide. This is the second ever outflow system, after the solar-type protostellar L1157 outflow, where multiple iCOMs have been detected using interferometers. Our main conclusions are the following:

- As in the case of L1157-B1 (Codella et al. 2017), iCOMs are not homogeneously distributed across the IRAS 4A outflows: methanol is more widespread over the two outflows, while acetaldehyde emission is only bright in the southern lobes, and dimethyl ether and formamide are concentrated in a spot at the (apparent) interface between the southern lobes of the 4A1 and 4A2 outflows. We therefore advise that derivation of iCOM abundance ratios from single-dish observations could be hazardous.
- The measured methanol to acetaldehyde abundance ratio is twice as large in the 4A1 outflow with respect to that in the 4A2 outflow; the comparison between these results with model predictions suggests that 1) the 4A1 outflow is younger than the 4A2 one and 2) acetaldehyde is synthesized in the gas phase by the reaction of atomic oxygen with ethyl radical. Alternatively, the grain mantle distribution might vary widely on small scales, which seems unlikely since the larger scale 4A2 outflow shows a similar $\text{CH}_3\text{OH}/\text{CH}_3\text{CHO}$ value in two distant points of the southern and northern lobes.

- Considering the $\text{CH}_3\text{OH}/\text{CH}_3\text{CHO}$ abundance ratio, the two IRAS 4A outflows show a sharp difference with respect to the L1157-B1 outflow. This may indicate that either the grain mantles or the gas volume densities are very different in the two regions. Additional observations are necessary to better constrain the reason of the observed difference.
- The methanol to acetaldehyde abundance ratio in the solar-type hot corinos is at least ten times higher than in the IRAS 4A outflows, again pointing to different grain mantle composition or densities. Interestingly, we note that $\text{CH}_3\text{OH}/\text{CH}_3\text{CHO}$ tentatively decreases with increasing bolometric luminosity of the Class 0 hot corino; a possible reason could be the larger sizes of the hot corinos.

Acknowledgements. We are very grateful to all the IRAM staff, whose dedication allowed us to carry out the SOLIS project. This project has received funding from: (i) the European Research Council (ERC) under the European Union's Horizon 2020 research and innovation programme, for the Project "The Dawn of Organic Chemistry" (DOC), grant agreement No 741002. (ii) This work has been supported by the project PRIN-INAF 2016 The Cradle of Life - GENESIS-SKA (General Conditions in Early Planetary Systems for the rise of life with SKA). V.T. acknowledges the financial support from the European Union's Horizon 2020 research and innovation programme under the Marie Skłodowska-Curie grant agreement n. 664931. C.F. acknowledges support from the French National Research Agency in the framework of the Investissements d'Avenir program (ANR-15- IDEX-02), through the funding of the "Origin of Life" project of the Univ. Grenoble-Alpes

References

- Altwegg, K., Balsiger, H., Bar-Nun, A., et al. 2016, *Sci. Adv.*, **2**, e1600285
- Arce, H. G., Santiago-García, J., Jørgensen, J. K., Tafalla, M., & Bachiller, R. 2008, *ApJ*, **681**, L21
- Bachiller, R., Guilloteau, S., Gueth, F., et al. 1998, *A&A*, **339**, L49
- Balucani, N., Ceccarelli, C., & Taquet, V. 2015, *MNRAS*, **449**, L16
- Bennett, C. J., Jamieson, C. S., Osamura, Y., & Kaiser, R. I. 2005a, *ApJ*, **624**, 1097
- Bennett, C. J., Osamura, Y., Lebar, M. D., & Kaiser, R. I. 2005b, *ApJ*, **634**, 698
- Bianchi, E., Codella, C., Ceccarelli, C., et al. 2017, *A&A*, **606**, L7
- Bianchi, E., Codella, C., Ceccarelli, C., et al. 2019, *MNRAS*, **483**, 1850
- Blake, G. A., Sandell, G., van Dishoeck, E. F., et al. 1995, *ApJ*, **441**, 689
- Boogert, A. C. A., Gerakines, P. A., & Whittet, D. C. B. 2015, *ARA&A*, **53**, 541
- Bottinelli, S., Ceccarelli, C., Lefloch, B., et al. 2004, *ApJ*, **615**, 354
- Burkhardt, A. M., Shingledecker, C. N., Le Gal, R., et al. 2019, *ApJ*, **881**, 32
- Castets, A., Ceccarelli, C., Loinard, L., Caux, E., & Lefloch, B. 2001, *A&A*, **375**, 40
- Cazaux, S., Tielens, A. G. G. M., Ceccarelli, C., et al. 2003, *ApJ*, **593**, L51
- Ceccarelli, C., Castets, A., Loinard, L., Caux, E., & Tielens, A. G. G. M. 1998, *A&A*, **338**, L43
- Ceccarelli, C., Caselli, P., Herbst, E., Tielens, A. G. G. M., & Caux, E. 2007, *Protostars and Planets V* (Tucson, AZ: University of Arizona Press), 47
- Ceccarelli, C., Caselli, P., Fontani, F., et al. 2017, *ApJ*, **850**, 176
- Charnley, S. B. 2004, *Adv. Space Res.*, **33**, 23
- Charnley, S. B., Tielens, A. G. G. M., & Millar, T. J. 1992, *ApJ*, **399**, L71
- Choi, M. 2001, *ApJ*, **553**, 219
- Choi, M. 2005, *ApJ*, **630**, 976
- Choi, M., Kang, M., Tatematsu, K., Lee, J.-E., & Park, G. 2011, *PASJ*, **63**, 1281
- Codella, C., Fontani, F., Ceccarelli, C., et al. 2015, *MNRAS*, **449**, L11
- Codella, C., Ceccarelli, C., Caselli, P., et al. 2017, *A&A*, **605**, L3
- Codella, C., Ceccarelli, C., Bianchi, E., et al. 2020, *A&A*, **635**, A17
- Coutens, A., Jørgensen, J. K., van der Wiel, M. H. D., et al. 2016, *A&A*, **590**, L6
- De Simone, M., Codella, C., Testi, L., et al. 2017, *A&A*, **599**, A121
- De Simone, M., Ceccarelli, C., Codella, C., et al. 2020, *ApJ*, **896**, L3
- Di Francesco, J., Myers, P. C., Wilner, D. J., Ohashi, N., & Mardones, D. 2001, *ApJ*, **562**, 770
- Elsila, J. E., Glavin, D. P., & Dworkin, J. P. 2009, *Meteorit. Planet. Sci.*, **44**, 1323
- Enrique-Romero, J., Rimola, A., Ceccarelli, C., & Balucani, N. 2016, *MNRAS*, **459**, L6

- Enrique-Romero, J., Rimola, A., Ceccarelli, C., et al. 2019, *ACS Earth Space Chem.*, **3**, 2158
- Garrod, R. T. 2008, *A&A*, **491**, 239
- Garrod, R. T., & Herbst, E. 2006, *A&A*, **457**, 927
- Goldsmith, P. F., & Langer, W. D. 1999, *ApJ*, **517**, 209
- Gueth, F., Guilloteau, S., & Bachiller, R. 1996, *A&A*, **307**, 891
- Herbst, E. 2017, *Int. Rev. Phys. Chem.*, **36**, 287
- Herbst, E., & van Dishoeck, E. F. 2009, *ARA&A*, **47**, 427
- Holdship, J., Viti, S., Codella, C., et al. 2019, *ApJ*, **880**, 138
- Jacobsen, S. K., Jørgensen, J. K., Di Francesco, J., et al. 2019, *A&A*, **629**, A29
- Jørgensen, J. K., van der Wiel, M. H. D., Coutens, A., et al. 2016, *A&A*, **595**, A117
- Jørgensen, J. K., Müller, H. S. P., Calcutt, H., et al. 2018, *A&A*, **620**, A170
- Karska, A., Herczeg, G. J., van Dishoeck, E. F., et al. 2013, *A&A*, **552**, A141
- Kirchhoff, W. H., Johnson, D. R., & Lovas, F. J. 1973, *J. Phys. Chem. Ref. Data*, **2**, 1
- Kleiner, I., Lovas, F. J., & Godefroid, M. 1996, *J. Phys. Chem. Ref. Data*, **25**, 1113
- Kristensen, L. E., van Dishoeck, E. F., Bergin, E. A., et al. 2012, *A&A*, **542**, A8
- Lay, O. P., Carlstrom, J. E., & Hills, R. E. 1995, *ApJ*, **452**, L73
- Lefloch, B., Castets, A., Cernicharo, J., Langer, W. D., & Zylka, R. 1998, *A&A*, **334**, 269
- Lefloch, B., Ceccarelli, C., Codella, C., et al. 2017, *MNRAS*, **469**, L73
- Loison, J.-C., Wakelam, V., & Hickson, K. M. 2014, *MNRAS*, **443**, 398
- Looney, L. W., Mundy, L. G., & Welch, W. J. 2000, *ApJ*, **529**, 477
- López-Sepulcre, A., Sakai, N., Neri, R., et al. 2017, *A&A*, **606**, A121
- Marcelino, N., Gerin, M., Cernicharo, J., et al. 2018, *A&A*, **620**, A80
- Maury, A. J., André, P., Testi, L., et al. 2019, *A&A*, **621**, A76
- Mendoza, E., Lefloch, B., López-Sepulcre, A., et al. 2014, *MNRAS*, **445**, 151
- Millar, T. J., Herbst, E., & Charnley, S. B. 1991, *ApJ*, **369**, 147
- Müller, H. S. P., Schlöder, F., Stutzki, J., & Winnewisser, G. 2005, *J. Mol. Struct.*, **742**, 215
- Nesterenok, A. V. 2018, *Astrophys. Space Sci.*, **363**, 151
- Neustock, W., Guarnieri, A., Demaison, J., & Włodarczak, G. 1990, *Z. Naturforsch. A*, **45**, 702
- Öberg, K. I., Garrod, R. T., van Dishoeck, E. F., & Linnartz, H. 2009, *A&A*, **504**, 891
- Öberg, K. I., van der Marel, N., Kristensen, L. E., & van Dishoeck, E. F. 2011, *ApJ*, **740**, 14
- Ospina-Zamudio, J., Lefloch, B., Ceccarelli, C., et al. 2018, *A&A*, **618**, A145
- Ospina-Zamudio, J., Lefloch, B., Favre, C., et al. 2019, *MNRAS*, **490**, 2679
- Padovani, M., Marcowith, A., Hennebelle, P., & Ferrière, K. 2016, *A&A*, **590**, A8
- Pickett, H. M., Poynter, R. L., Cohen, E. A., et al. 1998, *J. Quant. Spectr. Rad. Transf.*, **60**, 883
- Pizzarello, S., Cooper, G. W., & Flynn, G. J. 2006, *Meteorites and the Early Solar System II* (Tucson, AZ: University of Arizona Press), 625
- Podio, L., Lefloch, B., Ceccarelli, C., Codella, C., & Bachiller, R. 2014, *A&A*, **565**, A64
- Podio, L., Codella, C., Gueth, F., et al. 2016, *A&A*, **593**, L4
- Santangelo, G., Codella, C., Cabrit, S., et al. 2015, *A&A*, **584**, A126
- Skouteris, D., Vazart, F., Ceccarelli, C., et al. 2017, *MNRAS*, **468**, L1
- Skouteris, D., Balucani, N., Ceccarelli, C., et al. 2018, *ApJ*, **854**, 135
- Smith, K. W., Bonnell, I. A., Emerson, J. P., & Jenness, T. 2000, *MNRAS*, **319**, 991
- Taquet, V., Ceccarelli, C., & Kahane, C. 2012a, *A&A*, **538**, A42
- Taquet, V., Ceccarelli, C., & Kahane, C. 2012b, *ApJ*, **748**, L3
- Taquet, V., López-Sepulcre, A., Ceccarelli, C., et al. 2015, *ApJ*, **804**, 81
- Taquet, V., Codella, C., De Simone, M., et al. 2020, *A&A*, **637**, A63
- Tielens, A. G. G. M., & Hagen, W. 1982, *A&A*, **114**, 245
- Turner, B. E. 1990, *ApJ*, **362**, L29
- Vasyunin, A. I., Caselli, P., Dulieu, F., & Jiménez-Serra, I. 2017, *ApJ*, **842**, 33
- Watanabe, N., & Kouchi, A. 2002, *ApJ*, **571**, L173
- Xu, L.-H., Fisher, J., Lees, R., et al. 2008, *J. Mol. Spectr.*, **251**, 305
- Zucker, C., Schlawly, E. F., Speagle, J. S., et al. 2018, *ApJ*, **869**, 83